Distributed thin film sensor array for damage detection and localization

Austin Downey[a], Simon Laflamme[a,b] and Filippo Ubertini[c]

[a]Department of Civil, Construction, and Environmental Engineering, Iowa State University, Ames, IA, USA;
[b]Department of Electrical and Computer Engineering, Iowa State University, Ames, IA, USA;
[c]Department of of Civil and Environmental Engineering, University of Perugia, Perugia, Umbria, Italy;

ABSTRACT

The authors have developed a capacitive-based thin film sensor for monitoring strain on mesosurfaces. Arranged in a network configuration, the sensing system is analogous to a biological skin, where local strain can be monitored over a global area. The measurement principle is based on a measurable change in capacitance provoked by strain. In the case of bidirectional in-plane strain, the sensor output contains the additive measurement of both principal strain components. In this paper, we present an algorithm for retrieving unidirectional strain from the bidirectional measurements of the capacitive-based thin film sensor when place in a hybrid dense sensor network with state-of-the-art unidirectional strain sensors. The algorithm leverages the advantages of a hybrid dense network for application of the thin film sensor to reconstruct the surface strain maps. A bidirectional shape function is assumed, and it is differentiated to obtain expressions for planar strain. A least squares estimator (LSE) is used to reconstruct the planar strain map from the networks measurements, after the system's boundary conditions have been enforced in the model. The coefficients obtained by the LSE can be used to reconstruct the estimated strain map. Results from numerical simulations and experimental investigations show good performance of the algorithm.

Keywords: structural health monitoring, capacitive-based sensor, soft elastomeric capacitor, flexible membrane sensor, sensor network, signal decomposition, damage detection, damage localization.

1. INTRODUCTION

Structural health monitoring (SHM) of large-scale systems, here termed mesosystems, which include aerospace structures, energy systems and civil infrastructures, using off-the-shelf sensing systems is challenging due to the inherent geometric size and complexity of the monitored systems.[1] SHM may lead to strong economic benefits by enabling condition-based maintenance (CBM), instead of the traditional time-based or breakdown-based maintenance strategies. Of interest is the field of wind energy system, where CBM is known to have substantial economic benefits.[2–4]

Ideally, monitoring solutions for mesoscale structures would be capable of global (e.g., diagnosing overall health, change in boundary condition) and local (e.g., localizing material de-lamination, loosening of bolt, crack) condition assessment over strategic locations. However, differentiating between local and global changes for the detection and localization of damages using existing technologies and methods is difficult.[5,6] Linking transducer signals to condition assessment is often complicated by signal crosstalk and the dependence of the materials to environmental effects such as temperature and humidity.[7,8] It follows that detecting local damage at a global scale necessitates a large array of sensors,[9] which is difficult to financially justify.[10]

A solution to such local-global monitoring method is to deploy large-area electronics (LAEs), which have recently gained popularity with advances in the field of flexible electronics.[1,11] Their measurement principle

Further author information: (Send correspondence to Austin Downey)
Austin Downey: E-mail: adowney2@iastate.edu

is typically based on monitoring local states over global areas by deploying large arrays of flexible sensing substrates, analogous to sensing skins. State-of-the-art research in LAE includes large sensing sheets of strain gauges with embedded processors on polyimide sheet,[12,13] as well as resistance-based thin-films sensors bases on carbon nanotubes.[14,15] LAEs have been proposed for measuring strain,[16] pressure,[17] triaxial force,[18] and humidity.[19] While promising for mesoscale monitoring, LAE can be difficult to produce, or economically hard to justify in large volumes. In particular, there is a trade-off between the cost of a LAE's conductive filler and the electromechanical sensitivity of the sensor. The use of highly conductive nanoparticles, such as carbon nanotubes, can pose serious fabrication issues, primarily related with the difficult dispersion of the nanofiller, leading to a complex, and expensive fabrication process.[20]

The authors have previous proposed a new LAE based on soft elastomeric capacitors (SECs). The SEC technology was designed to be inexpensive and easy to fabricate, mechanically robust, and customizable in shapes and sizes.[21,22] The SEC is fabricated from an inexpensive nanocomposite based on a styrene-co-ethylene-co-butylene-co-styrene (SEBS) block co-polymer matrix filled with titania (dielectric) and carbon black (electrodes) particles. In previous work, the static[21] and dynamic[1,23] behaviors of the SEC have been characterized, and dense network application for fatigue crack detection demonstrated.[24]

As it will be discussed later, a particular feature of the SEC is that it measures additive in-plane strain, instead of a traditional single-axis measurement. In many dense sensor network (DSN) applications of the SEC, such as for the extraction of strain maps over a large surface, it is necessary to decompose the strain into its principal components. In previous work, an algorithm was developed to leverage the DSN configuration to enable such decomposition.[25] The algorithm assumed a shape function and classical Kirchhoff plate theory and used a least squares estimator (LSE) to find the coefficients of the shape function. While numerical simulations showed the promise of the algorithm, conclusions were made that the technique was limited by the quality of the assumptions on the boundary conditions, which are difficult to assume for complex geometries.

In this paper, the authors build on previous work on the strain decomposition algorithm[25] and propose a hybrid DSN (HDSN) to alleviate the additive strain limitation of the SEC. The HDSN includes resistive strain gauges (RSGs), a mature technology capable of precise point measurements but can hardly cover a large surface due to technical and economical constraints.[26] It combines the advantages of mesosurface coverage capacity of the SEC and high precision measurements from the RSGs. The LSE-based algorithm explained above is extended to include RSG readings and uses different weighted matrices to concatenate data in the algorithm, allowing for the enforcement of localized strain conditions and the fusion of unidirectional and bidirectional strain sensors into a global strain map. These algorithmic improvements also build a basis for future work in real-time boundary condition updating and regression fitting of parameters weights. Simulations and laboratory verification of the proposed HDSN are performed on a cantilever plate combining 20 SECs and 16 RSGs (plus 16 additional RSGs for validation purposes).

The paper is organized as follows. Section 2 introduces the SEC sensory system including the SEC's electromechanical model. Section 3 introduces a revised LSE algorithm applicable for use in a HDSN. The updated LSE algorithm and application methodology is presented and a HDSN is introduced in section 4. Section 5 reports and discusses algorithm results for both the simulation and experiential validation. Lastly, section 7 concludes the paper.

2. BACKGROUND

The SEC is a novel LAE sensing solution for strain sensing over mesosurfaces. The sensor is fabricated using an SEBS block co-polymer matrix, filled with titania to form the dielectric. The same SEBS is filled with carbon black particles to form the conductive plates. The resulting sensor is an inexpensive flexible capacitor, which can be customized in shapes or sizes. Figure 1 shows three different sizes of square SECs compared to a commercial RSG (gauge length of 5 mm).

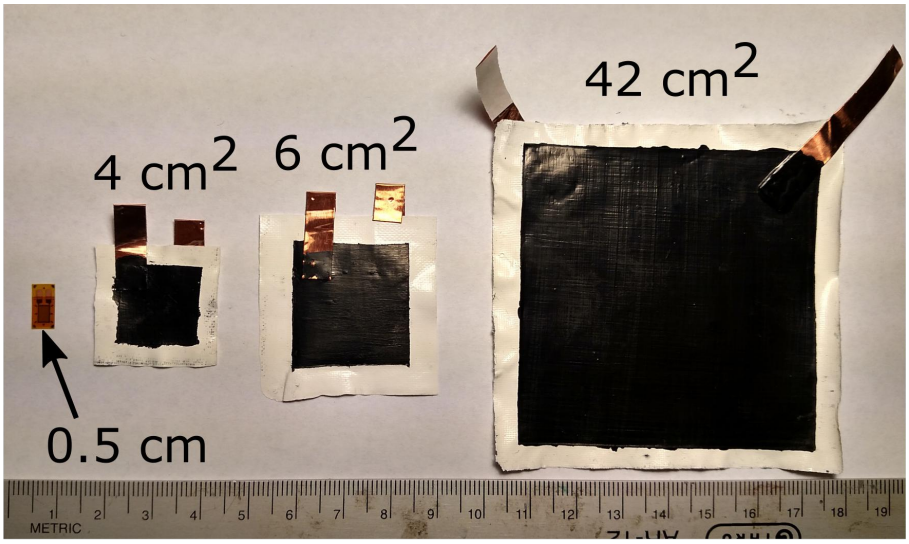

Figure 1: commercial RSG compared to three different sizes of square SECs

2.1 Electro-Mechanical model

The SEC is designed to measure in-plane strain ($x-y$ plane in Fig. 2) by adhering the sensor onto the monitored surface using an off-the-shelf epoxy. Assuming a low sampling rate (< 1 kHz), the SEC can be modeled as a non-lossy capacitor with capacitance C

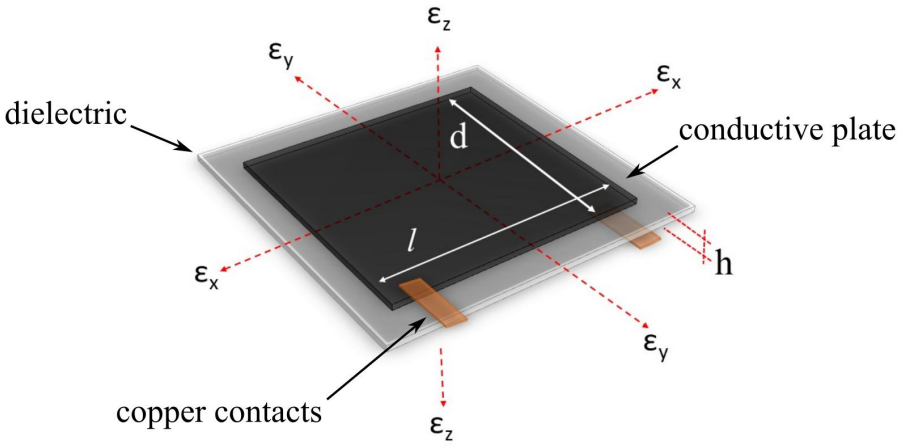

Figure 2: sketch of a SEC's geometry with reference axes

$$C = e_0 e_r \frac{A}{h} \tag{1}$$

where $e_0 = 8.854$ pF/m is the vacuum permittivity, e_r is the polymer relative permittivity, $A = d \cdot l$ is the sensor area of width d and length l, and h is the thickness of the dielectric. Assuming small strain, one can take the differential of Eq. (1)

$$\frac{\Delta C}{C} = \left(\frac{\Delta l}{l} + \frac{\Delta w}{w} - \frac{\Delta t}{t} \right) = \varepsilon_x + \varepsilon_y - \varepsilon_z \tag{2}$$

where ε_x, ε_y and ε_z are strains in the x, y and z directions as shown in Fig. 2. An expression relating ε_z to ε_x and ε_y can be obtained using Hooke's law for in-plane stress

$$\varepsilon_z = -\frac{\nu}{1-\nu}(\varepsilon_x + \varepsilon_y) \tag{3}$$

yielding

$$\frac{\Delta C}{C} = \lambda(\varepsilon_x + \varepsilon_y) \tag{4}$$

where $\lambda = \frac{1}{1-\nu}$ represents the gauge factor of the sensor. For SEBS, $\nu \approx 0.49$,[27] which gives a gauge factor $\lambda \approx 2$. Equation (4) shows that the signal of the SEC varies as a function of the additive strain $\varepsilon_x + \varepsilon_y$. The linearity of the derived electro-mechanical model is valid for mechanical loading frequencies of less than 15 Hz.[1] A nonlinear version of the model is presented in[23] valid up to 40 Hz.

3. STRAIN DECOMPOSITION ALGORITHM

In this section, an extension to the strain decomposition algorithm previously proposed[25] is presented. The LSE-based algorithm is modified to include data from unilateral strain sensors (the RSGs) for the enforcement of localized strain conditions.

As discussed in section 2.1, the SEC signal includes the additive in-plane strain components. The algorithm for surface strain reconstruction proposed by Wu et. al.[25] consists of assuming a shape function, enforcing the boundary conditions, and computing the coefficients of the shape function using an LSE. A polynomial shape function of the type $\sum^n b_{ij}x^i y^j$ showed promise for conducting strain decomposition on a simulated wind turbine blade. Consider a cantilever plate as illustrated in Fig. 3, and an n^{th} order polynomial to approximation of its deflection shape w

$$\begin{aligned} w(x,y) &= \sum_{i=2,j=2}^{n} b_{ij}x^i y^j \\ &= \mathbf{HB} \end{aligned} \tag{5}$$

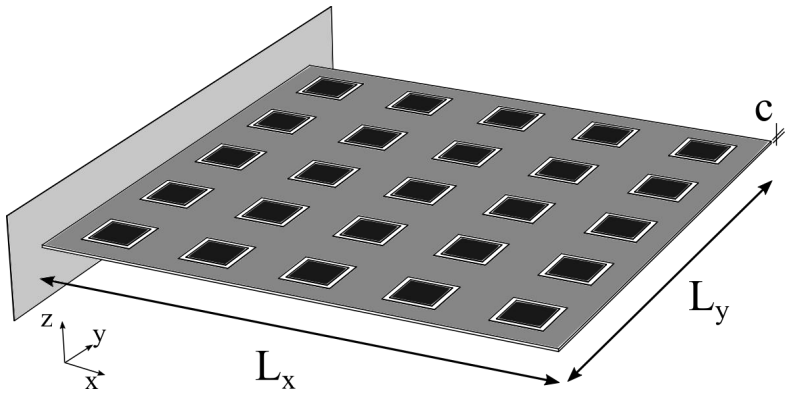

Figure 3: cantilever plate with 20 SECs

where w is the deflection of the plate at point (x, y) and b_{ij} are constants. In matrix form, $\mathbf{H}$ is termed the sensor placement matrix and $\mathbf{B}$ the fitting coefficients matrix. Assuming elastic deformations and the validity of Kirchhoff's plate theory, the surface strain $\varepsilon_x, \varepsilon_y$ can be obtained from Equation (4) as a function of the sensor signal matrix $\mathbf{S}$,

$$\mathbf{S} = [\mathrm{s}_1 ... \mathrm{s}_k ... \mathrm{s}_m]^{\mathrm{T}} = -\frac{c}{2}\frac{\partial \mathbf{W}}{\partial x^2} - \frac{c}{2}\frac{\partial \mathbf{W}}{\partial y^2} \tag{6}$$

where $s = \Delta C/(\lambda C) = \varepsilon_x + \varepsilon_y$, c is the plate thickness and $\mathbf{W}$ is a vector containing vertical displacements at sensors' locations. The unidirectional strains are written

$$\begin{aligned} \varepsilon_x(x, y) &= -\frac{c}{2}\frac{\partial^2 w}{\partial x^2} = \mathbf{H}_{\mathrm{x}}\mathbf{B}_{\mathrm{x}} \\ \varepsilon_y(x, y) &= -\frac{c}{2}\frac{\partial^2 w}{\partial y^2} = \mathbf{H}_{\mathrm{y}}\mathbf{B}_{\mathrm{y}} \end{aligned} \tag{7}$$

To enforce boundary conditions on the SECs and incorporate RSG data into the algorithm, two diagonal matrices (Γ_{x} and Γ_{y}) are introduced in the $\mathbf{H}_{\mathrm{x}}$ and $\mathbf{H}_{\mathrm{y}}$ matrices

$$\begin{aligned} \left[\frac{\mathbf{S}_{\mathrm{SEC}}}{\mathbf{S}_{\mathrm{RSG}}}\right] &= \left[\ \boldsymbol{\Gamma}_{\mathrm{x}}\mathbf{H}_{\mathrm{x}} \mid \boldsymbol{\Gamma}_{\mathrm{y}}\mathbf{H}_{\mathrm{y}}\ \right]\left[\frac{\mathbf{B}_{\mathrm{x}}}{\mathbf{B}_{\mathrm{y}}}\right] \\ &= \mathbf{H}_{\mathrm{xy}}\mathbf{B} \end{aligned} \tag{8}$$

where $\mathbf{S}_{\mathrm{SEC}}$ and $\mathbf{S}_{\mathrm{RSG}}$ compose the signal vector $\mathbf{S}$, composed of the SEC and RSG signals respectively. In this configuration, if Γ_{x} and Γ_{y} are taken as weighted identity matrices, $\mathbf{H}_{\mathrm{xy}}$ is collinear and $\mathbf{H}_{\mathrm{xy}}^{\mathrm{T}}\mathbf{H}_{\mathrm{xy}}$ singular. It follows that some entries in $\mathbf{H}$ need to be altered, which is done by enforcing boundary conditions directly in the matrix. This is done by selecting the appropriate weight parameters $\gamma_{\mathrm{x},k}$ and $\gamma_{\mathrm{y},k}$ associated with sensor k. For instance, in the case of a cantilever plate, the boundary condition along the fixity can be assumed as $\varepsilon_y(0, a_y \leq y \leq L_y - a_y) = 0$, where a_y is a positive constants such that $0 \leq a_y \leq L_y$ to account for different boundary conditions at corners. This assumed boundary condition is enforced for the SECs along the fixity using $\gamma_{\mathrm{x},m} = 1$, $\gamma_{\mathrm{y},m} = 0$. Similarly, RSG signals are incorporated in $\mathbf{H}$ using

$$\gamma_{\mathrm{x},k} = 1 \ , \ \gamma_{\mathrm{y},k} = 0 \tag{9}$$

if the k-th RSG measures strain along the x-axis, or alternatively

$$\gamma_{\mathrm{x},k} = 0 \ , \ \gamma_{\mathrm{y},k} = 1 \tag{10}$$

Different weight values other than unity can be selected in the design of γ to add more weight on fitting given sensors. The fitting coefficients are estimated using an LSE

$$\hat{\mathbf{B}} = (\mathbf{H}_{\mathrm{xy}}^{\mathrm{T}}\mathbf{H}_{\mathrm{xy}})^{-1}\mathbf{H}_{\mathrm{xy}}^{\mathrm{T}}\mathbf{S} \tag{11}$$

where the hat denotes an estimation. It follows that the strain maps can be reconstructed using

$$\hat{\varepsilon}_x = \mathbf{H}_{\mathrm{x}}\hat{\mathbf{B}}_{\mathrm{x}} \qquad \hat{\varepsilon}_y = \mathbf{H}_{\mathrm{y}}\hat{\mathbf{B}}_{\mathrm{y}} \tag{12}$$

4. METHODOLOGY

Validation of the strain decomposition algorithm presented in Section 3 is conducted numerically and experimentally using an HDSN approach. This section introduces the experimental HDSN configuration, presents the finite element model (FEM) used for the numerical simulations and the experimental procedures, and lists the algorithm parameters and shape functions under study.

4.1 Experimental HDSN configuration

A HDSN consisting of 20 SECs and 32 RSGs, 16 of which are used for validation of the results only, is constructed for experimental validation. The HDSN is mounted on a fiberglass plate of geometry 74 cm $\times$ 63 cm with a thickness of 0.32 cm and a fixity along one edge as shown in Fig. 4(a). Figure 4(b) shows a schematic of the sensor placement. Each SEC covers an area of 42 cm^2, and are laid out in a 4 $\times$ 5 grid array. The center of each SEC is taken as the sensor node in constructing the **H** matrix. RSGs are Cu-Ni alloy foils manufactured by Tokyo Sokki Kenkyujo, model FLA-6-350-11-3LT, with a gauge length of 6 mm. They are aligned along the plate's principle axes, individually measuring ε_x and ε_y as indicated in Fig. 4(b) by red circles and blue squares, respectively. Table 1 lists measuring axis for each RSG, and whether the sensor is used within the model or for validation of the results.

Table 1: RSG configuration

ε	LSE and validation	validation only
ε_x	x1, x3, x6, x8, x10, x11, x13, x15	x2, x4, x5, x7, x9, x12, x14, x16
ε_y	y2, y3, y6, y8, y10, y11, y12, y115	y1, y4, y5, y7, y9, y13, y14, y16

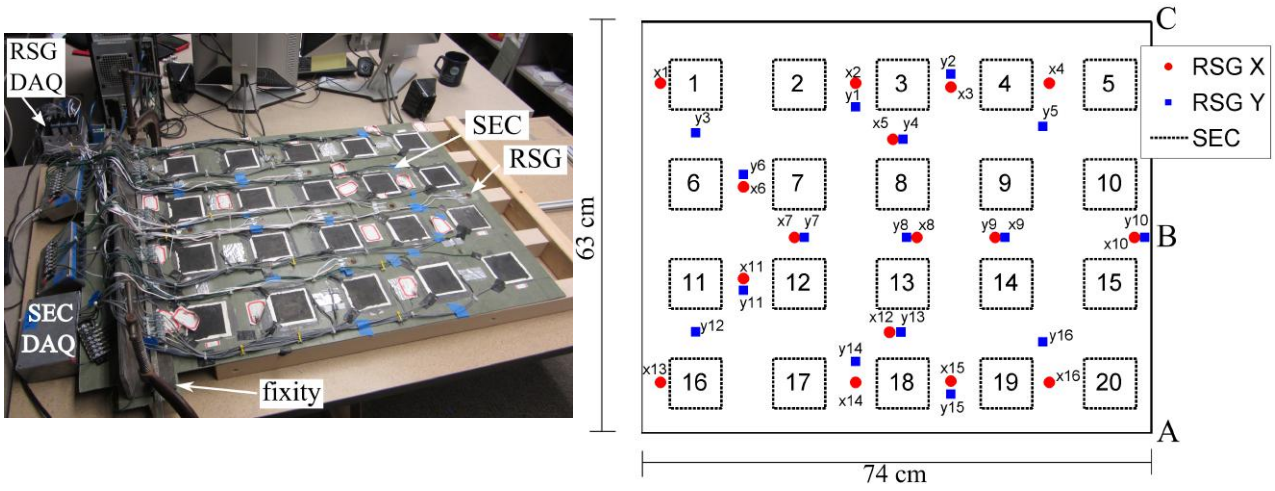

(a) (b)

Figure 4: HDSN: (a) experimental setup; and (b) sensor nomenclature

The plate is subjected to three different displacement-controlled loads, listed in Table 2. Case 1 consists of a roller support along the free edge $\overline{AC}$, while load cases 2 and 3 are point supports at points B and C, shown in Fig. 4(b).

Table 2: Loading cases

case	point	displacement
1	$\overline{\text{AC}}$	125 mm
2	B	150 mm
3	C	150 mm

The data acquisition (DAQ) hardware is annotated in Fig. 4 for both the SEC (inside protective boxes) and the RSG signals. SEC measurements are recorded using a capacitance to digital converter, PCAP-02, manufactured by ACAM-Messelectronic GmbH. The acquisition of data was performed using a PCAP-02 evaluation board with ACAM's proprietary software at a sampling rate of 25 Hz. RSG measurements are recorded using a National Instruments cDAQ-9174 with three 24-bit 350 Ω quarter-bridge modules (NI-9236) through LabVIEW, sampled at 50 Hz.

During testing, a limited number of SECs (1 to 2) were found to exhibit abnormal drift in the signal, possibly attributed to electromagnetic (EMI) noise. EMI noise is difficult to completely eliminate with the SEC. Thus, when a sensor showed excessive drift in its signal, it was declared as faulty and its signal replaced by the mean of adjacent SECs.

4.2 Finite element model

Numerical simulations of the HDSN were performed on an FEM of the plate in Abaqus. The model assumed a plate of constant isotropic material properties and thickness. Five thousand of four-node stress/displacement shell elements with reduced integration and five integration points through the plates thickness were used to discretize the FEM. The model had displacement and rotational degrees of freedom, while shear deformation was ignored. Material constants where obtained experimentally from material drops. The resulting Young's Modulus was 15 GPa, the Poisson's ratio 0.21, and the density 4.5 g/cm^3.

4.3 Algorithm properties

A polynomial function (Eq. (5)) for the deflection shape was assumed. A 4-th order polynomial was selected to improve the ability of the strain decomposition algorithm in capturing strain features in the y direction, and the terms x^2y^5 and y^5 where added to the shape function to improve the fitting accuracy, such that

$$w(x,y) = \sum_{i=2,j=2}^{4} a_{ij}x^i y^j + x^2y^5 + y^5 \tag{13}$$

Selection of the weight parameters γ was conducted to enforce some boundary conditions and to fuse RSG data into the algorithm. They are summarized in Table 3.

For the boundary conditions along the fixity, ε_y was assumed to be zero for $a_y \leq y \leq L_y - a_y$, where $a_y = 0.2$m to account for the plate's edge effects. This is enforced in the LSE algorithm by setting $\gamma_{\text{y},1}$ and $\gamma_{\text{y},16}$ to zero. A similar approach was taken for ε_y at the plate's free corners (SEC 5 and 20) due to the low level of strain present; again, ε_y was enforced as zero by setting $\gamma_{y,5}$ and $\gamma_{y,20}$ to zero. In addition, for loading case 3 that introduced a high level of rotation to the plate, $\gamma_{y,1}$ was set to zero.

For the integration of RSG data, each γ for the principal strain normal to the sensor's measurement axis was set to zero. Lastly, all weight parameters for the RSGs were scaled by a factor of 2 to account for the higher precision of the off-the-shelf sensors.

Table 3: Weight parameters γ

		load case					
		1		2		3	
	sensor number	γ_x	γ_y	γ_x	γ_y	γ_x	γ_y
SECs	1	1	1	1	1	1	1
	2	1	1	1	1	1	0
	3,4	1	1	1	1	1	1
	5	1	0	1	0	1	0
	6	1	0	1	0	1	0
	7 to 10	1	1	1	1	1	1
	11	1	0	1	0	1	0
	12 to 19	1	1	1	1	1	1
	20	1	0	1	0	1	0
RSGs	x_1 to x_{16}	2	0	2	0	2	0
	y_1 to y_{16}	0	2	0	2	0	2

5. RESULTS

Results from the numerical and experimental validations are presented and discussed in this section.

5.1 Numerical simulations

Simulated sensor data for the HDSN were extracted from the FEM. SEC strain was taken as the average value of the summation of strain $\varepsilon_x + \varepsilon_y$ for all elements that fell completely within the SEC's footprint. RSG strain was extracted from the FEM element corresponding to the RSG's location.

Figures 5 to 7 are plots of the decomposed strain maps using the strain decomposition algorithm. Values are compared against the FEM results. The strain maps are reconstructed by calculating the strain using equation 12 for each sensor node used to construct **H**. Strain values between sensor nodes are obtained by assuming a first order fit.

The performance of the algorithm's output is quantified using the mean absolute percent error (MAPE) between both strain maps. The computation of the MAPE is conducted at the RSG sensor nodes to provide a reference between the simulated and experimental data presented in Section 5.3. Another MAPE is calculated using every element in the FEM field that lies within the HDSN's 4×5 SEC grid. This subset was selected to eliminate the high discrepancies between the FEM and the LSE outside the HDSN. Strains outside the HDSN are not considered in the algorithm's formulation. The MAPE results for the numerical simulations (0%) are presented in Table 4.

Generally, the LSE algorithm provides an acceptable level of error for the reconstruction of the unidirectional strain within the HDSN. Loading cases 1 and 2 provide better strain decomposition in terms of MAPE. In particular, the algorithm is fairly accurate at reproducing the y coordinate strain maps for this simple loading case (figure 6(b)). Higher order responses are filtered out by the LSE algorithm, resulting in continuous strain maps and allowing the LSE algorithm to naturally filter the sensors' signals. Capturing the higher order strain shape around the point load presented in loading case 2 would require an altered shape function and denser sensor network around the location of the point load. A greater discrepancy can be seen in figure 7 for the corner load (case 3). The LSE strain map shows a considerable divergence from the FEM estimated strain map due to the asymmetry in the plate's response and the sparseness of the sensor network along the free edge. The ability of the LSE algorithm to capture features along the HDSN's edge needs further investigation. In general, the LSE algorithm did slightly worse at decomposing each loading case's strain along the y coordinate (ε_y), possibly explained by the higher complexity of the strain map and lower number of SECs in that particular direction.

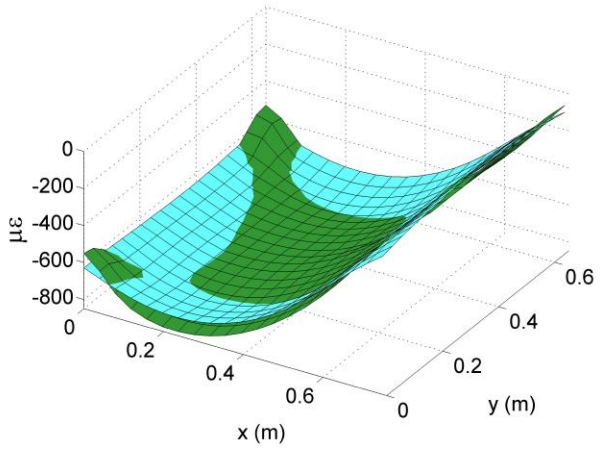

(a)

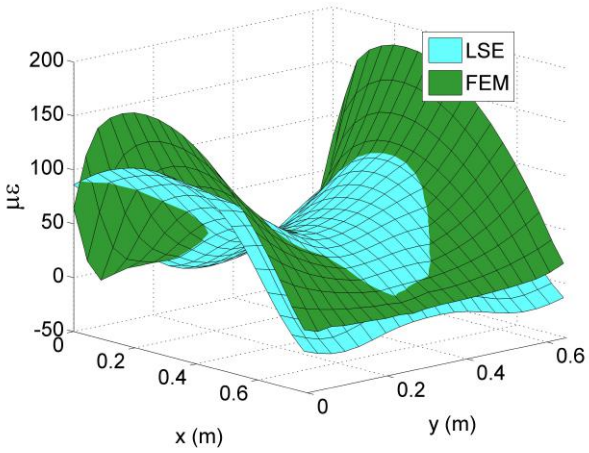

(b)

Figure 5: loading case 1 (roller support on free edge): (a) decomposed x strain map; and (b) decomposed y strain map

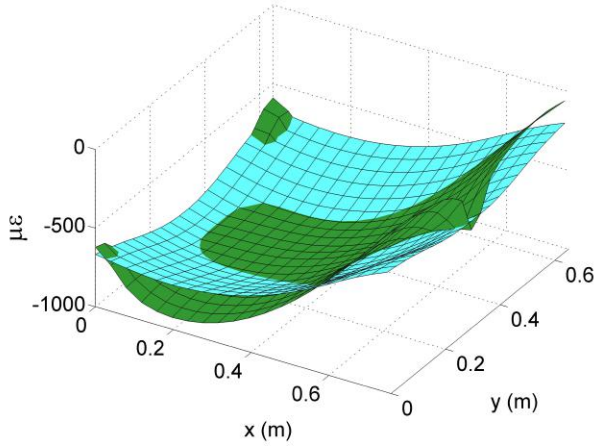

(a)

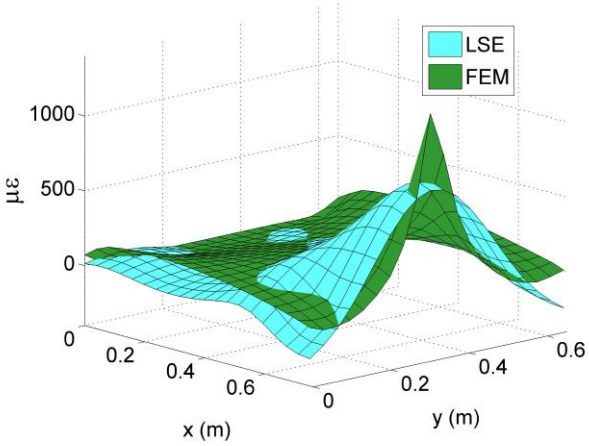

(b)

Figure 6: loading case 2 (center point on free edge): (a) decomposed x strain map; and (b) decomposed y strain map.

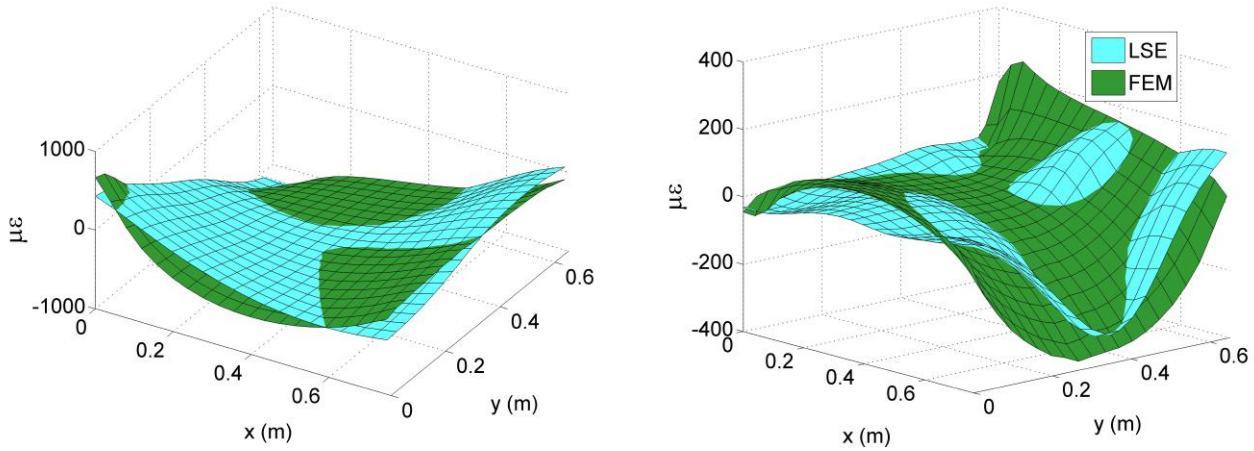

(a) (b)

Figure 7: loading case 3 (corner point on free edge): (a) decomposed x strain map; and (b) decomposed y strain map.

5.2 Robustness to noise

To evaluate the robustness of the algorithm with respect to noise, a noise signature is extracted from experimental data, amplified, and added to the sensors' signals to simulate a real-word operating environment (e.g., inside a wind turbine blade). Time series data for an SEC under loading case 1 was selected to investigate the SEC noise signature. SEC 17 was selected due to its relatively high strain level ($\approx 800\ \mu\varepsilon$) and characteristic response. The time-domain capacitance signal is shown in figure 8 for an unloaded-loaded-unloaded test, where the spike in the signal around 17 seconds is due to a repositioning of the plate on the roller support. Data for constructing the SEC's noise signature is extracted from the steady-state, loaded portion of the test, over the 18 - 29 sec range.

The distribution of the extracted SEC signal is plotted in Fig. 9(a) with a normal (Gaussian) distribution centered at $\mu = -0.715$ pF and standard deviation $\sigma = 0.044$ pF. The ability of a normal distribution to effectively estimate the signal noise is demonstrated in Fig. 9(b). Thus, a standard deviation of $\sigma = 0.044$ is deemed appropriate for conducting simulations on the effects of noise. The simulated response as a function of the introduced Gaussian white noise is presented in Figs. 10 to 12 for every loading cases and both MAPE metrics. The algorithm noise response results where calculated using the average of 1000 simulated iterations per noise level. Table 4 summarizes the simulation results for selected noise levels.

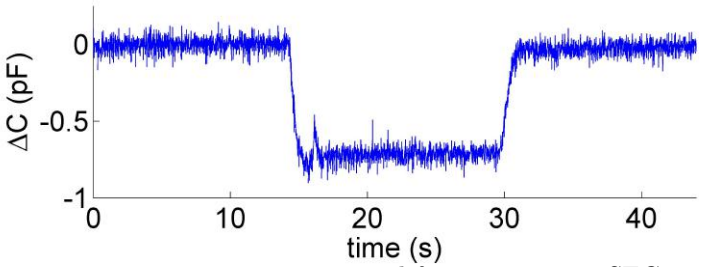

Figure 8: time series sensor response used for constructing SEC noise signature

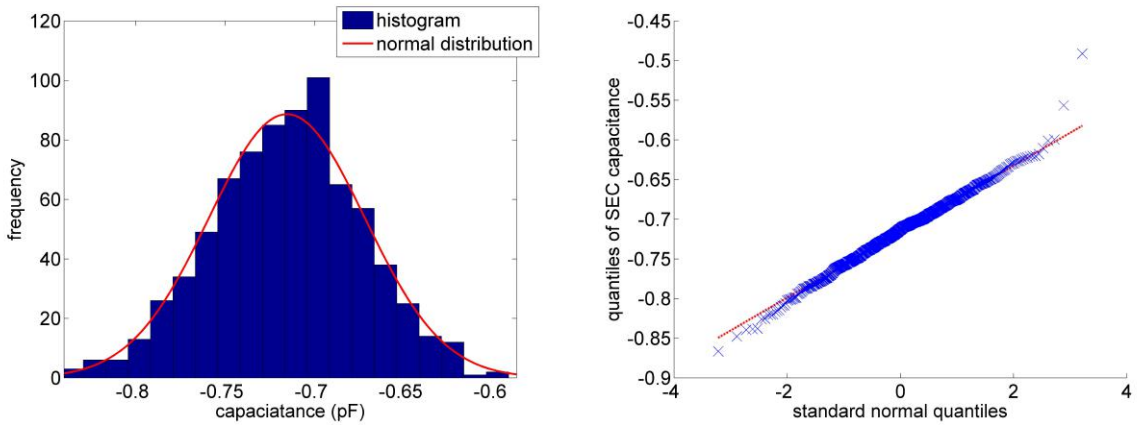

Figure 9: SEC noise investigation: (a) histogram of SEC sensor signal; and (b) QQ-plot against the normal distribution.

The introduction of noise into the LSE algorithm generally degrades the fitting performance, except for load case 1 for the fitting of ε_y at the location of the RSGs. Nevertheless, noise in this particular case provoked a significant increase in the MAPE variance (Fig. 10(a)).

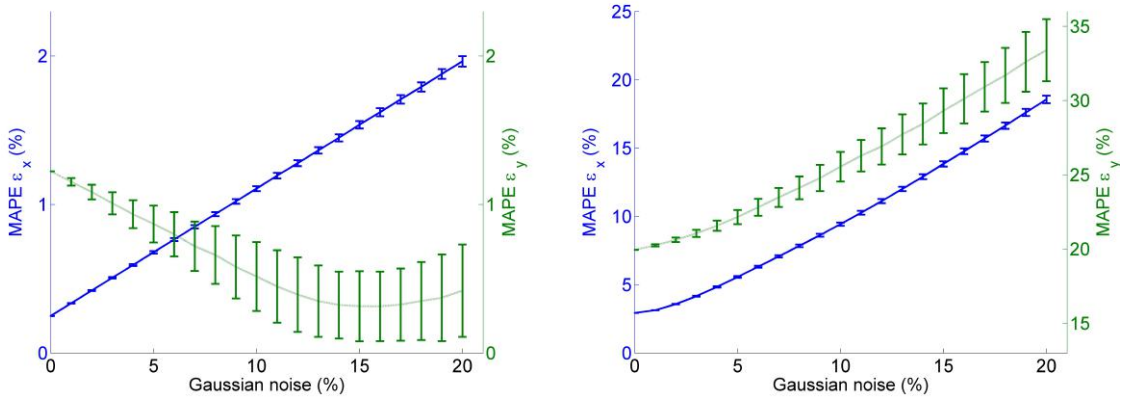

(a) (b)

Figure 10: MAPE vs noise for loading case 1 (roller support on free edge); the error bars denote ± standard deviation intervals computed among 1000 simulation results per noise realizations: (a) at RSG locations; and (b) at FEM node location.

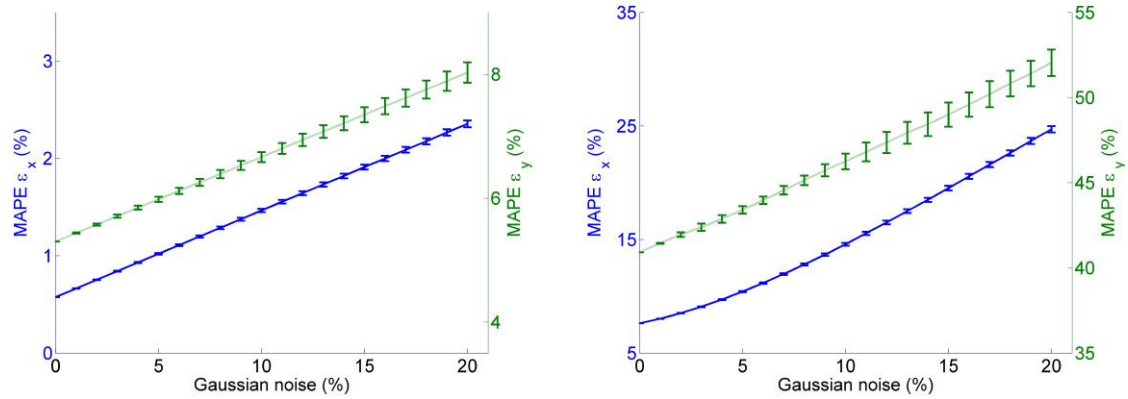

(a) (b)

Figure 11: MAPE vs noise for loading case 2 (center point on free edge); the error bars denote ± standard deviation intervals computed among 1000 simulation results per noise realizations: (a) at RSG locations; and (b) at FEM node location.

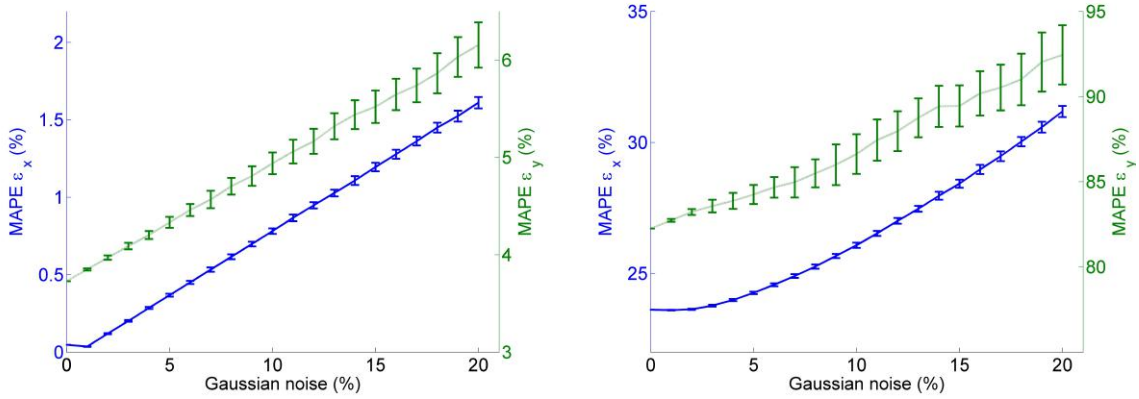

(a) (b)

Figure 12: MAPE vs noise for loading case 3 (corner point on free edge); the error bars denote ± standard deviation intervals computed among 1000 simulation results per noise realizations: (a) at RSG locations; and (b) at FEM node location.

Table 4: Simulation results

		Gaussian noise							
		0 %		1 %		5 %		10 %	
loading case	ε	LSE-RSG MAPE	LSE-FEM MAPE	LSE-RSG MAPE	LSE-FEM MAPE	LSE-RSG MAPE	LSE-FEM MAPE	LSE-RSG MAPE	LSE-FEM MAPE
1	ε_x	0.2	2.9	0.3	3.1	0.7	5.6	1.1	9.4
	ε_y	1.2	19.9	1.1	20.2	0.9	22.2	0.5	25.5
2	ε_x	0.6	7.6	0.7	8.0	1.0	10.4	1.4	14.6
	ε_y	5.3	40.9	5.4	41.5	6.0	43.4	6.6	45.5
3	ε_x	0.0	23.6	0.1	23.6	0.4	24.3	0.8	26.1
	ε_y	3.7	82.3	3.8	82.7	4.3	84.25	4.9	86.6

5.3 Experimental results

Experimental validation for the HDSN was performed on the laboratory setup shown in Fig. 4. Figures 13 - 15 show the unidirectional strain maps for all three loading cases.

Two different MAPE metrics are investigated: 1) a comparison of fitting versus all RSGs; and 2) a comparison of fitting versus the 16 RSGs used for validation only, which are not present in the formulation of **H**. The FEM constructed for the numerical simulations is not used to validate the LSE algorithm against the RSG data, due to large discrepancies in matching the RSG data with the actual model. These discrepancies are possibly due to the non-modeled wires, clips, sensors, and protective tape, and to the non-ideal fixity, heterogeneous material properties, and inconsistent plate geometry. An enhanced FEM model could offer benefits for validation of the experimental results discussed in section 5.3. This task is left to future work.

Results from the experimental investigation lead to similar conclusions as for the numerical simulations. Here, the LSE-based algorithm shows great agreement with data from the RSGs, whether it is compared against all RSGs or just the 16 RSGs used for validation. The better performance (MAPE) provided by a comparison with all RSGs is due to the integration of some of the RSG data directly in the algorithm. Load case 2 (point load, center) yields abnormally high MAPE for fitting of the strain along the y-axis (ε_y), which may be attributed to the higher order map necessary to characterize the strain behavior, as concluded with the numerical investigation.

Table 5: LSE algorithm results

loading case	ε	LSE - All RSG MAPE	LSE - Validation RSG MAPE
1	ε_x	0.23	0.45
	ε_y	1.61	3.24
2	ε_x	0.34	0.68
	ε_y	22.2	44.3
3	ε_x	0.19	0.38
	ε_y	0.50	1.01

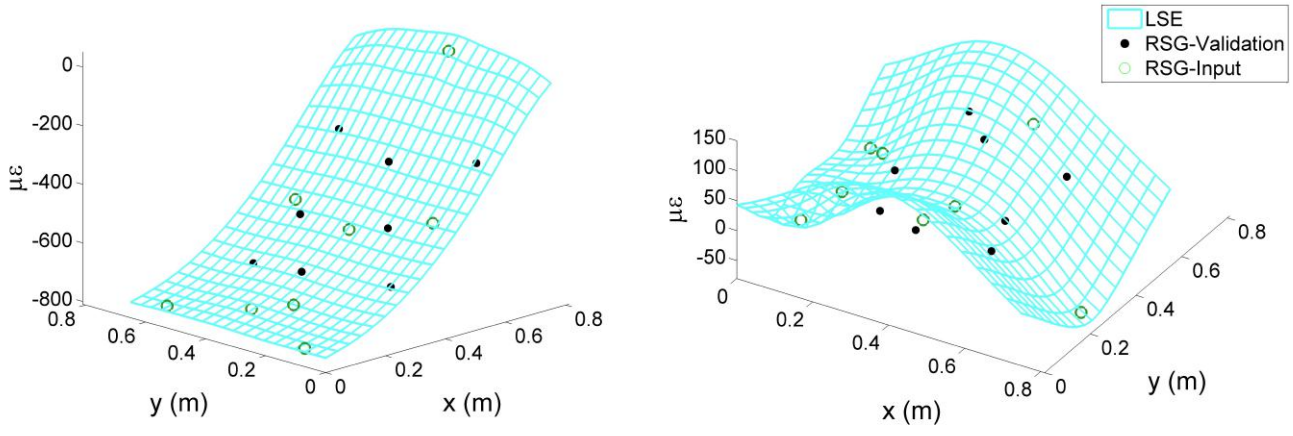

(a) (b)

Figure 13: loading case 1 (roller support on free edge): (a) decomposed x strain map; and (b) decomposed y strain map.

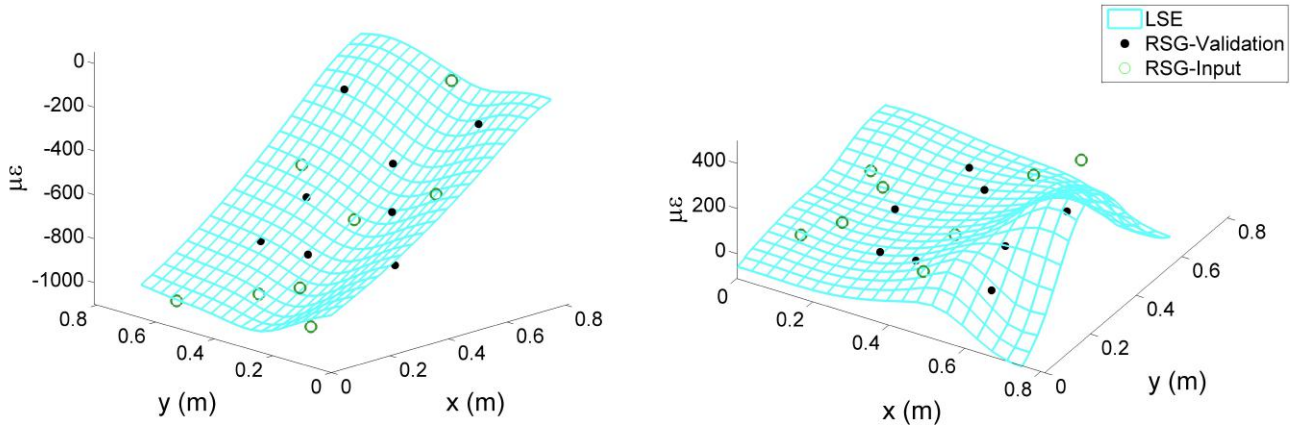

(a) (b)

Figure 14: loading case 2 (center point on free edge): (a) decomposed x strain map; and (b) decomposed y strain map.

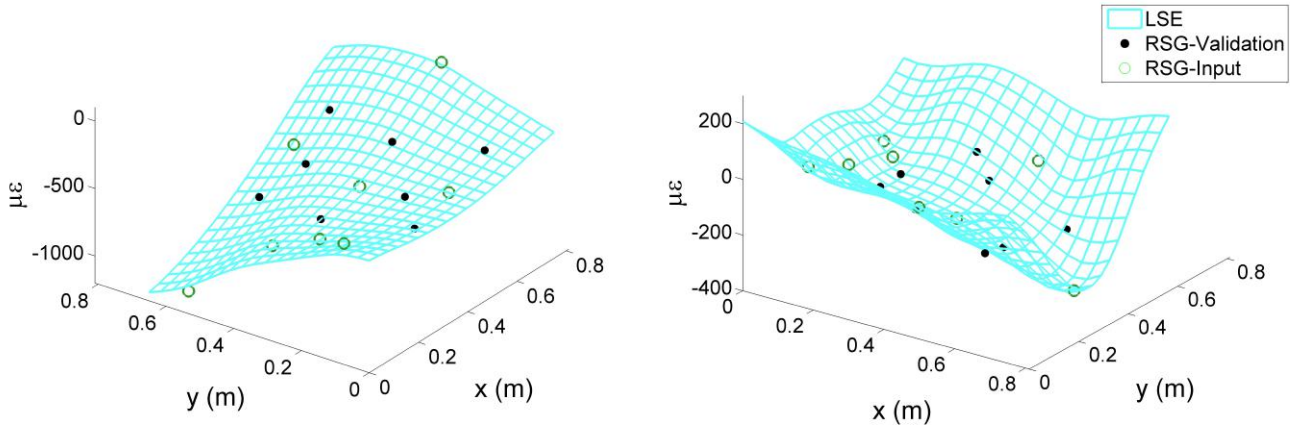

(a) (b)

Figure 15: loading case 3 (corner point on free edge): (a) decomposed x strain map; and (b) decomposed y strain map.

6. CONCLUSION

This paper has presented an extended LSE-based algorithm for decomposing in-plane strain present in the additive signal of a novel sensor, the soft elastomeric capacitor (SEC). The SEC is a large-scale strain gauge, designed to cover large surfaces at low cost. The extension is based on a hybrid dense network application (HDSN), in which the SEC technology is combined with mature off-the-shelf technology, here the resistive strain gauge (RSG), to improve the strain decomposition capabilities. The previously proposed LSE-based algorithm consisted of assuming a shape function and classical Kirchhoff plate theory, and using a least squares estimator (LSE) to find the coefficients of the shape function. The extended version presented in this paper included weighted matrices to concatenate data from both the SECs and the RSGs, allowing for the enforcement of localized strain conditions and the fusion of unidirectional and bidirectional strain sensors into a global strain map.

Numerical and experimental investigations were conducted on a cantilever plate equipped with 20 SECs and 32 RSGs, 16 of which were used for validation. For a plate under the simple loading cases under investigation, the LSE algorithm successfully produced unidirectional strain maps. However, it showed limitations in fitting high order strain maps, possibly due to the limited number of SECs used in the investigation. Future investigation is needed to validate the algorithms for use with an expanded library of loading cases, applied over different locations of the HDSN. Sensor network design, including the number and placement of sensors needs to be explored. This includes the use of asymmetric sensor networks and the inclusion of SECs of different geometries.

Results presented show the promise of the technology for monitoring large-scale surfaces, such as wind turbine blades and aircraft wings by leveraging a hybrid sensor network configuration. For example, a HDSN could be used to extract global unidirectional strain maps and deflection shapes on a global surface to create high fidelity finite element models, while the SECs could be used to extract discrete information on a global surface, such as local damage in the form of fatigue cracks.

Acknowledgments

The development of the SEC technology is supported by grant No. 13-02 from the Iowa Energy Center. This work is also partly supported by the National Science Foundation Grant No.1069283, which supports the activities of the Integrative Graduate Education and Research Traineeship (IGERT) in Wind Energy Science, Engineering and Policy (WESEP) at Iowa State University. Their support is gratefully acknowledged.

REFERENCES

1. Simon Laflamme, Filippo Ubertini, Hussam Saleem, Antonella DAlessandro, Austin Downey, Halil Ceylan, and Annibale Luigi Materazzi. Dynamic characterization of a soft elastomeric capacitor for structural health monitoring. *Journal of Structural Engineering*, 141(8):04014186, 2015.
2. Peter C Chang, Alison Flatau, and SC Liu. Review paper: health monitoring of civil infrastructure. *Structural health monitoring*, 2(3):257–267, 2003.
3. Chia Chen Ciang, Jung-Ryul Lee, and Hyung-Joon Bang. Structural health monitoring for a wind turbine system: a review of damage detection methods. *Measurement Science and Technology*, 19(12):122001, 2008.
4. Douglas Adams, Jonathan White, Mark Rumsey, and Charles Farrar. Structural health monitoring of wind turbines: method and application to a hawt. *Wind Energy*, 14(4):603–623, 2011.
5. Y Zou, LPSG Tong, and GP Steven. Vibration-based model-dependent damage (delamination) identification and health monitoring for composite structuresa review. *Journal of Sound and vibration*, 230(2):357–378, 2000.
6. Filippo Ubertini, Annibale Luigi Materazzi, Antonella DAlessandro, and Simon Laflamme. Natural frequencies identification of a reinforced concrete beam using carbon nanotube cement-based sensors. *Engineering structures*, 60:265–275, 2014.
7. Erik Gross, Todd Simmermacher, Mark Rumsey, and Rick I Zadoks. Application of damage detection techniques using wind turbine modal data. In *American Society of Mechanical Engineers Wind Energy Symp.(Reno, NV, USA)*, pages 99–0047, 1999.
8. Mark A Rumsey and Joshua A Paquette. Structural health monitoring of wind turbine blades. In *The 15th International Symposium on: Smart Structures and Materials & Nondestructive Evaluation and Health Monitoring*, pages 69330E–69330E. International Society for Optics and Photonics, 2008.
9. Chia Chen Ciang, Jung-Ryul Lee, and Hyung-Joon Bang. Structural health monitoring for a wind turbine system: a review of damage detection methods. *Measurement Science and Technology*, 19(12):122001, 2008.
10. Dan M Frangopol and Thomas B Messervey. Life-cycle cost and performance prediction: role of structural health monitoring. *Frontier technologies for infrastructures engineering: structures and infrastructures book series*, 4:361, 2009.
11. John A Rogers, Takao Someya, and Yonggang Huang. Materials and mechanics for stretchable electronics. *Science*, 327(5973):1603–1607, 2010.

12. Yingzhe Hu, Warren S Rieutort-Louis, Josue Sanz-Robinson, Liechao Huang, Branko Glisic, James C Sturm, Steffen Wagner, Naveen Verma, et al. Large-scale sensing system combining large-area electronics and cmos ics for structural-health monitoring. *Solid-State Circuits, IEEE Journal of*, 49(2):513–523, 2014.
13. ST Tung, Y Yao, and B Glisic. Sensing sheet: the sensitivity of thin-film full-bridge strain sensors for crack detection and characterization. *Measurement Science and Technology*, 25(7):075602, 2014.
14. Limin Gao, Erik T Thostenson, Zuoguang Zhang, Joon-Hyung Byun, and Tsu-Wei Chou. Damage monitoring in fiber-reinforced composites under fatigue loading using carbon nanotube networks. *Philosophical Magazine*, 90(31-32):4085–4099, 2010.
15. Kenneth J Loh, Junhee Kim, Jerome P Lynch, Nadine Wong Shi Kam, and Nicholas A Kotov. Multifunctional layer-by-layer carbon nanotube–polyelectrolyte thin films for strain and corrosion sensing. *Smart Materials and Structures*, 16(2):429, 2007.
16. Michael Suster, Jun Guo, Nattapon Chaimanonart, Wen H Ko, and Darrin J Young. A high-performance mems capacitive strain sensing system. *Microelectromechanical Systems, Journal of*, 15(5):1069–1077, 2006.
17. Darren J Lipomi, Michael Vosgueritchian, Benjamin CK Tee, Sondra L Hellstrom, Jennifer A Lee, Courtney H Fox, and Zhenan Bao. Skin-like pressure and strain sensors based on transparent elastic films of carbon nanotubes. *Nature nanotechnology*, 6(12):788–792, 2011.
18. Jagoda Anna Dobrzynska and MAM Gijs. Polymer-based flexible capacitive sensor for three-axial force measurements. *Journal of Micromechanics and Microengineering*, 23(1):015009, 2012.
19. PM Harrey, BJ Ramsey, PSA Evans, and DJ Harrison. Capacitive-type humidity sensors fabricated using the offset lithographic printing process. *Sensors and Actuators B: Chemical*, 87(2):226–232, 2002.
20. Simon Laflamme, Hussam S Saleem, Mohamed Elkashef, Kejin Wang, and Eric Cochran. Conductive paint-filled cement paste sensor for accelerated percolation. In *SPIE Smart Structures and Materials+ Nondestructive Evaluation and Health Monitoring*, pages 943722–943722. International Society for Optics and Photonics, 2015.
21. S. Laflamme, H.S. Saleem, B.K. Vasan, R.L. Geiger, Degang Chen, M.R. Kessler, and K. Rajan. Soft elastomeric capacitor network for strain sensing over large surfaces. *Mechatronics, IEEE/ASME Transactions on*, 18(6):1647–1654, Dec 2013.
22. Simon Laflamme, Matthias Kollosche, Jerome J Connor, and Guggi Kofod. Robust flexible capacitive surface sensor for structural health monitoring applications. *Journal of Engineering Mechanics*, 139(7):879–885, 2012.
23. Hussam Saleem, Austin Downey, Simon Laflamme, Matthias Kollosche, and Filippo Ubertini. Investigation of dynamic properties of a novel capacitive-based sensing skin for nondestructive testing. *Materials Evaluation*, 73(10):1390–1397, 2015.
24. Sari Kharroub, Simon Laflamme, Chunhui Song, Daji Qiao, Brent Phares, and Jian Li. Smart sensing skin for detection and localization of fatigue cracks. *Smart Materials and Structures*, 24(6):065004, 2015.
25. Jingzhe Wu, Chunhui Song, Hussam S Saleem, Austin Downey, and Simon Laflamme. Network of flexible capacitive strain gauges for the reconstruction of surface strain. *Measurement Science and Technology*, 26(5):055103, 2015.
26. Wenyi Liu, Baoping Tang, and Yonghua Jiang. Status and problems of wind turbine structural health monitoring techniques in china. *Renewable Energy*, 35(7):1414–1418, 2010.
27. A.N. Wilkinson, M.L. Clemens, and V.M. Harding. The effects of sebs-g-maleic anhydride reaction on the morphology and properties of polypropylene/pa6/sebs ternary blends. *Polymer*, 45(15):5239 – 5249, 2004.